J. Quant. Spectrosc. Radiat. Transfer Vol. 43, No. 2, pp. 133–148, 1990
Printed in Great Britain.

0022-4073/90 $3.00 + 0.00

RADIATIVE TRANSFER IN STRATIFIED ATMOSPHERES: DEVELOPMENT AND VERIFICATION OF A UNIFIED MODEL

SI-CHEE TSAY† and KNUT STAMNES‡
Geophysical Institute and Department of Physics, University of Alaska-Fairbanks, Fairbanks, AK 99775-0800, U.S.A.

KOLF JAYAWEERA
Department of Physics, University of Alaska-Fairbanks, Fairbanks, AK 99775-1240, U.S.A.

(*Received* 20 *June* 1989)

Abstract—A reliable and efficient discrete method is verified for multiple scattering, radiative-transfer calculations in vertically inhomogeneous, non-isothermal atmospheres in local thermodynamic equilibrium. The linear-in-optical-depth approximation to the Planck function is used to obtain accurate solutions for thermal radiation. We show that this approximation significantly improves computing efficiency while still maintaining adequate accuracy. Using this multiple-scattering scheme, we have constructed and validated a radiation model for stratified atmospheres, taking into account molecular (Rayleigh) scattering and absorption/emission. The exponential sum fitting of transmissions technique is utilized to parameterize gaseous absorption, thereby achieving a unified treatment of shortwave and longwave radiative transfer. To validate the model, we present computed fluxes and heating/cooling rate profiles for the five McClatchey atmospheres. The results are compared with other models having different spectral resolution (Δs) and gaseous scattering and absorption/emission structure. Specifically, we compare broad-band ($\Delta s > 100\,\text{cm}^{-1}$), narrow-band ($\Delta s < 100\,\text{cm}^{-1}$) and line-by-line computations and find that at the expense of accuracy by a few W-m^{-2} for flux or a few tenth °C/day for heating/cooling rate computations, the broad-band models are very fast and may be suitable for many applications. We also find that in spite of good agreement between fluxes (at the top and bottom boundaries) computed by different methods, the heating/cooling rate profiles may differ substantially due to compensating errors.

1. INTRODUCTION

Estimation of the radiative energy budget of planetary atmospheres and determination of atmospheric heating/cooling rates require integrations over the solar as well as the planetary radiation spectra. For atmospheres in which infrared (i.r.) scattering can not be ignored, the most efficient and accurate but perhaps not the most common way to do this is to reduce the problem to a series of monochromatic computations.

The degree of sophistication of the radiative transfer solution depends primarily on the desired level of accuracy. If our interest lies primarily in the global energy balance, the planetary albedo is of utmost importance. For problems involving atmospheric dynamics we must compute the local heating/cooling rate profile which is proportional to the divergence of the net flux or the mean intensity (i.e., intensity averaged over 4π sr). The mean intensity is also needed in order to compute atmospheric photodissociation rates which are of vital importance in photochemical models aimed at investigating the evolution of atmospheric ozone. Thus, for problems involving global or local energy balance and photochemical reaction rates, the angular intensity or radiance is not required; it suffices to determine integrated quantities such as fluxes (irradiances) and mean intensities (integrated radiance) in such cases. The angular intensity, on the other hand, contains information

†Present address: Department of Atmospheric Science, Colarado State University, Fort Collins, CO 80523, U.S.A.
‡To whom all correspondence should be addressed.

about the composition and state of a planetary atmosphere and is the quantity of interest for most remote sensing applications. For example, it is the measured backscattered ultraviolet (u.v.) solar intensity that is used to infer the atmospheric ozone content from satellites (Heath et al[1]).

Angular intensity calculations are usually much more time-consuming than flux and mean intensity calculations. Thus, from a practical point of view, methods of solving the transfer equation should be made flexible to meet various needs. It would therefore be desirable to have available reliable and efficient techniques for solving the equation of transfer for monochromatic radiation in which the desired level of accuracy can be tailored (at the expense of computing cost) to meet the requirements of any particular problem at hand. Here we have adopted one such technique, namely, the discrete ordinate method described in some detail elsewhere.[2]

In this paper, we focus on clear-sky computations and parameterization of gaseous absorption by the three main trace gases: water vapor, carbon dioxide, and ozone, as well as Rayleigh scattering. Subjects related to cloudy and hazy sky are presented in the work of Tsay et al.[3] We start in the following section with a brief summary of the solution to the radiative transfer equation and provide verifications of this solution procedure for applications to thermally emitting/scattering media in Sec. 3. In Sec. 4, we describe the solar and terrestrial radiation model including spectral structure and the technique utilized for incorporating molecular scattering and absorption/emission. In Sec. 5, we present results from different parameterizations of molecular scattering and absorption. We also compare results for different spectral resolutions and discuss the consequences of eliminating relatively unimportant gaseous absorption for fast computation. Accuracy considerations and a summary are presented in Sec. 6.

2. BASIC EQUATIONS AND SOLUTIONS

We now focus on the computation of heating/cooling rates for which only fluxes or mean intensities are needed. Thus, we may start with the azimuthally averaged version of the equation describing the transfer of diffuse monochromatic radiation at frequency ν in a scattering, absorbing and emitting plane-parallel atmosphere in LTE given by[4,5]

$$\mu \frac{\mathrm{d}u_\nu(\tau_\nu, \mu)}{\mathrm{d}\tau_\nu} = u_\nu(\tau_\nu, \mu) - \frac{\omega_\nu(\tau_\nu)}{4\pi} \int_{-1}^{1} P_\nu(\tau_\nu, \mu; \mu') u_\nu(\tau_\nu, \mu')\, \mathrm{d}\mu' - \frac{\omega_\nu(\tau_\nu) I_0}{4\pi} P_\nu(\tau_\nu, \mu; -\mu_0) \exp(-\tau_\nu/\mu_0) - [1 - \omega_\nu(\tau_\nu)] B_\nu(T). \quad (1)$$

Here, θ is the polar angle and $\mu = \cos\theta$. We have made the usual diffuse–direct distinction (Chandrasekhar,[4] p. 22) so that u_ν in Eq. (1) describes the azimuthally averaged diffuse intensity or radiance only. Thus, I_0 is the intensity of solar radiance incident in direction μ_0 so that $\mu_0 I_0$ is the incident vertical flux or irradiance. $\omega_\nu(\tau_\nu)$ is the single scattering albedo, $P_\nu(\tau_\nu, \mu; \mu')$ the azimuthally averaged scattering phase function, τ_ν the extinction optical depth and $B_\nu(T)$ the Planck function at frequency ν and temperature T. The second term on the rhs in Eq. (1) is due to multiple scattering, the third is a consequence of the diffuse–direct distinction and is called the solar pseudo-source, while the fourth term describes thermal emission.

Since planetary atmospheres, in general, and the Earth's atmosphere, in particular, consist of a mixture of various radiatively active gases and cloud and aerosol particles that have non-constant mixing ratios, the optical properties (i.e., the single scattering albedo and the phase function) vary with altitude or optical depth. To account for this inhomogeneity and the fact that real atmospheres are non-isothermal, we divide the atmosphere into a series of adjacent, homogeneous layers in which the scattering and absorbing properties are taken to be constant within each layer but are allowed to vary from layer to layer. Within each layer we adopt a linear-in-optical-depth variation of the Planck function.[6]

A variety of techniques exist for solving Eq. (1) and a recent review of such methods is provided in Ref. 5. Applying the discrete ordinate method,[2] we find that the intensity is given by

$$u_p(\tau, \mu_i) = \sum_{j=1}^{N} \{\tilde{C}_{jp} G_{jp}(\mu_i) \exp[-k_{jp}(\tau - \tau_{p-1})] + \tilde{C}_{-jp} G_{-jp}(\mu_i) \exp[-k_{jp}(\tau_p - \tau)]\} + Z_p(\mu_i) \exp(-\tau/\mu_0) + [Y_{0p}(\mu_i) + Y_{1p}\tau], \quad (2)$$

where the μ_i are the quadrature angles, $\tau_{p-1} \leqslant \tau \leqslant \tau_p$, and N is the number of discrete points utilized in each hemisphere when replacing the integral over angle in Eq. (1) by numerical quadrature. The $Y_{0p}(\mu_i)$ are determined by the optical and thermal properties of the layer. The eigenvalues k_{jp} and the eigenvectors $G_{jp}(\mu_i)$ depend on the optical properties of each layer. The C_{jp} are determined from boundary and continuity conditions and depend upon the incident solar radiation, the atmospheric thermal properties and the surface characteristics. $Z_p(\mu_i)\exp(-\tau/\mu_0)$ is the particular solution due to a parallel beam of solar radiation incident in direction $\theta_0 = \cos^{-1}\mu_0$. We refer to Ref. 2 for a complete and detailed account of the solution procedure. Since numerical validation of our theory for thermally emitting/scattering media is still lacking, however, we provide such verification in the following section.

To compute fluxes and heating/cooling rate, we use the formulas

$$F_v(\tau_v) = \int_0^{2\pi} d\phi \int_{-1}^{1} \mu u_v(\tau_v, \mu)\, d\mu = 2\pi \sum_{j=-N}^{N} w_i \mu_i u_v(\tau_v, \mu_i), \tag{3}$$

$$\frac{\partial T}{\partial t} = -\frac{1}{C_p \rho}\frac{\partial F_v}{\partial z}, \tag{4}$$

where ϕ refers to integration over the azimuth and w_i is the quadrature weight. T stands for temperature, t for time, C_p for specific heat at constant pressure p, ρ for mass density, z for geometric height and F_v for net flux at frequency v.

3. NUMERICAL VERIFICATION FOR THERMALLY EMITTING/SCATTERING MEDIA

In previous publications (Ref. 5 and references therein), we have verified our solutions extensively for solar radiation incident an anisotropically scattering, and vertically inhomogeneous atmospheres. We will therefore focus on thermal radiation below.

The thermal radiation term, $B(T)$ in Eq. (1), is often approximated by a constant value by assuming isothermal conditions for any given layer. A better approximation of the thermal radiation in which $B(\tau)$ is assumed to vary linearly with optical depth across any given layer was first considered by Schwarzschild[7] in a study of the equilibrium of the Sun's atmosphere. At a fixed wavelength in the i.r. regime, the Planck function depends exponentially on temperature whereas the temperature lapse rate decreases linearly with height in most convective atmospheres. For atmospheres in hydrostatic equilibrium the density decreases exponentially with height and the optical depth is proportional to the density. Thus,

$$B(T) \propto \exp(T) \propto \exp(-z) \propto \rho \propto \tau.$$

Wiscombe[6] examined quantitatively the maximum errors incurred in approximating the Planck function as linear in optical depth for conditions typical of the Earth's atmosphere. He showed that the averaged error of $B(\tau)$ with respect to $B(T)$ over a layer is quite small if ΔT and $\Delta\tau$ across this layer are properly chosen. Although this linear approximation has been used in various radiation schemes,[8-10] its performance and accuracy has to our knowledge never been investigated, within the framework of a radiation model. Below we focus on this issue.

To explore the accuracy of the isothermal and linear-in-optical-depth approximations we consider an atmosphere in which the temperature decreases linearly with height from 280 K at the bottom to 270 K at the top. Most of the emission occurs in the wavenumber range from 300 to 800 cm^{-1}, corresponding to the peak emission at these temperatures. The lower boundary is assumed to emit black-body radiation at a temperature of 280 K. The optical depth of this non-isothemal layer is varied from 0.1 to 100, covering transparent to opaque conditions. For simplicity the layer is assumed to be homogeneous with single scattering albedo ranging from 0.1 to 0.95 and the corresponding asymmetry factor from 0.05 to 0.75, representing the absorption/emission and scattering dominant regimes, respectively. Results from a 100-layer isothermal model in which the temperature in the middle of any sublayer is used to represent that layer and a 100-layer linear model agree very well (to the fourth decimal place), due to the small temperature across sublayers. Therefore, they are regarded as benchmark.

In Table 1, we compare flux and flux divergence computations using one-layer, linear and isothermal approximations with the benchmark 100-layer results. Four and 16 streams [$2N$ in Eqs. (2) and (3)] discrete ordinate solutions are shown. For upward and downward fluxes, the one-layer linear approximation generally yields an accuracy of about 0.05 W-m^{-2} (or 0.03%) for 16 streams and about 0.5 W-m^{-2} (or 0.3%) for four streams. In contrast, a 16-stream one-layer isothermal approximation systematically overestimates the upward flux at the top and underestimates the downward flux at the bottom. When the optical depth is small (transparent), the upward flux is essentially produced by the radiation emitted from the lower boundary. As the optical depth becomes larger, the absorption of the layer approaches saturation and quasi-black body behavior is observed. The failure of the one-layer isothermal approximation becomes more serious as the optical depth of the layer increases. This happens simply because the isothermal approximation overestimates the temperature at the top and underestimates the temperature at the bottom for a linearly decreasing temperature profile, when the temperature in the middle of the layer is used to represent the layer. For flux divergence (Table 1), the performance of the one-layer 16-stream isothermal approximation is somewhat improved due to compensating errors in upward and downward flux computations. The failure of the isothermal approximation will also worsen with increasing temperature difference across the layer. We have chosen a 10 K span within the layer for demonstration purposes, but some radiation models probably use a layering with larger temperature spans across layers. Therefore, the illustrations given here may in some sense be regarded as conservative estimates of the errors that would be incurred in actual models by using the isothermal approximation.

Table 2 shows critical errors of the upward and downward intensities at the top and the bottom of the layer. The critical error is defined as the maximum error among the eight quadrature angles relative to the 16-stream 100-layer model used as a benchmark. Positive critical errors represent overestimation and negative errors underestimation. Clearly, the one-layer linear approximation performs far better than does the one-layer isothermal approximation. Generally, intensities produced by the linear approximation agree with the benchmark 100-layer values to within 2–3 decimal places.

Table 1. Sensitivity and accuracy comparison of flux computation for thermal emission with various τ, $\omega = 0.1$, and $g = 0.05$ (in parentheses, for $\omega = 0.95$ and $g = 0.75$) in layer with temperature 270 K at the top and 280 K at the bottom. The Planck fluxes at wavenumber interval from 300 to 800 cm^{-1} are 160.81 and 179.85 W m^{-2} at the top and bottom, respectively.

(a) Upward flux at the top

τ	Linear-in-τ, 4-stream, 1-layer	Linear-in-τ, 16-stream, 1-layer	Isothermal, 16-stream, 1-layer	Benchmark, 16-stream, 100-layer
0.1	176.94 (173.89)	177.08 (174.65)	177.14 (174.65)	177.07 (174.65)
1.0	167.05 (148.15)	167.17 (149.64)	169.10 (149.71)	167.11 (149.63)
10.	158.74 (107.55)	158.80 (107.59)	166.71 (109.30)	158.78 (107.55)
100	157.57 (101.96)	157.63 (102.02)	166.71 (107.36)	157.63 (102.01)

(b) Flux divergence in layer

τ	Linear-in-τ, 4-stream, 1-layer	Linear-in-τ, 16-stream, 1-layer	Isothermal, 16-stream, 1-layer	Benchmark, 16-stream, 100-layer
0.1	-25.46 (-1.60)	-24.62 (-1.60)	-24.59 (-1.59)	-24.60 (-1.59)
1.0	-119.54 (-14.89)	-120.23 (-14.92)	-120.05 (-14.90)	-120.12 (-14.90)
10.	-157.44 (-84.00)	-157.50 (-84.06)	-157.27 (-83.94)	-157.45 (-83.99)
100	-157.44 (-101.37)	-157.50 (-101.43)	-157.27 (-101.28)	-157.50 (-101.40)

Table 2. As in Table 1 except for showing critical errors of intensity at quadrature angles with corresponding Planck intensities of 51.19 and 57.25 W m^{-2} sr^{-1} for top and bottom, respectively.

(a) Upward intensity at the top

τ	Linear-in-τ 16-stream	Isothermal 16-stream
0.1	0.01~0.08% (0.00~0.01%)	0.01~3.36% (0.00~0.35%)
1.0	0.03~0.09% (0.01~0.02%	0.57~5.42% (0.01~0.99%)
10.	-0.03~0.07% (0.06~0.08%	4.67~5.76% (1.18~2.87%)
100	-0.05~0.01% (0.02~0.06%)	5.73~5.78% (5.20~5.44%)

(b) Downward intensity at bottom

τ	Linear-in-τ 16-stream	Isothermal 16-stream
0.1	0.08~0.10% (0.01~0.04%)	-0.05~-3.11% (0.01~-0.31%)
1.0	0.06~0.10% (0.01~0.05%	-0.84~-4.74% (-0.01~-0.51%)
10.	0.06~0.08% (0.02~0.06%)	-4.20~-4.98% (-0.85~-1.24%)
100	0.06~0.10% (0.02~0.05%)	-5.01~-5.12% (-1.51~-3.39%)

Table 3. Comparisons of flux computation with doubling method for various τ, ω, and g in a layer of temperature 270 K at top and 280 K at bottom. Planck fluxes in wavenumber interval from 1 to 10^5 cm are 301.35 and 348.53 W m^{-2} for top and bottom, respectively.

Upward flux at the top

τ	ω	g	Linear-in-τ 4-stream	Linear-in-τ 16-stream	Doubling 16-stream
0.1	0.05	0.05	343.15	343.37	343.37
	0.50	0.50	337.77	338.60	338.60
	0.95	0.75	336.94	338.41	338.41
	1.00	0.80	337.88	339.55	339.55
1.0	0.05	0.05	321.72	321.93	321.93
	0.50	0.50	305.52	306.49	306.49
	0.95	0.75	286.57	289.46	289.46
	1.00	0.80	287.25	291.15	291.15
10.	0.05	0.05	301.47	301.53	301.53
	0.50	0.50	280.31	280.99	280.99
	0.95	0.75	204.78	204.85	204.85
	1.00	0.80	136.45	135.59	135.59
100	0.05	0.05	298.61	298.66	298.66
	0.50	0.50	276.27	276.95	276.95
	0.95	0.75	191.44	191.54	191.54
	1.00	0.80	21.94	21.69	21.69

The doubling method is regarded as one of the most accurate methods (within 3–4 decimal places) for flux and azimuth-independent intensity computation.[11,12] To compare with doubling results we adopted the same atmospheric profile as for Table 1, except for the results being integrated over the 1–10^5 cm^{-1} spectral interval for both methods. Table 3 shows the comparison of the upward flux at the top for various values of optical depth, single scattering albedo and asymmetry factor. In general, the one-layer linear approximation for 16 streams yields results in very good agreement (within 3–4 digits) with those from the doubling method. Results from four-stream models have a flux difference of < 1.0 W-m^{-2}, except for the conservative cases.

During the Arctic stratus cloud experiment,[13] a frequently-observed phenomenon was the low level stratus cloud in the surface inversion layer. To describe the inversion layer, we adopt an atmospheric profile starting at the surface with a temperature of about 271.2 K and increasing to 279.2 K at 200 m above the surface. The St-II drop size distribution[14] is used to simulate the wavenumber dependence of the optical properties of the cloud, as shown in Table 4. Figure 1 shows the relative errors of fluxes and flux divergences for three one-layer approximations, using a 16-stream 100-layer model as benchmark. Computations are performed from 100 to 1300 cm^{-1} spectral interval, in which mid-points of each 100 cm^{-1} interval are chosen to represent that interval. Results similar to those of Table 1 are obtained, except that overestimation of the upward flux is replaced by underestimation for the one-layer isothermal approximation (and *vice versa* for the downward flux) because of the temperature inversion. Figure 2 shows the critical errors of intensities at the quadrature angles, which are also consistent with those shown in Table 2.

The average computer CPU time, in VAX-785, for the linear-in-optical-depth approximation is about 0.1 sec for a four-stream one-layer model, about 0.4 sec for a 16-stream one-layer model, and about 40 sec for a 16-stream 100-layer isothermal model. Clearly, the computer CPU times increase linearly with the number of layers. Thus, the linear-in-optical-depth approximation of the Planck function for thermal emission significantly improves computing efficiency while still maintaining accuracy. This is important because in climate models up to 90% of the total

Table 4. Optical parameters for flux calculations of an inversion layer in thermal emission of temperature 279.2 K at top [or $B(T_t) = 109.68$ W m^{-2} sr^{-1}] and 271.2 K at bottom [or $B(T_b) = 97.64$ W m^{-1} sr^{-1}]. ν (cm^{-1}) stands for wavenumber: λ (μm) for wavelength at center of interval; ω for single scattering albedo of droplet; g for asymmetry factor; I (%) for percentage of intensity over entire spectrum.

ν	0 - 100	100 - 200	200 - 300	300 - 400	400 - 500	500 - 600	600 - 700	700 - 800	800 - 900	900 - 1000	1000 - 1100	1100 - 1200	1200 - 1300	1300 - ∞
λ		66.0	40.0	28.5	22.2	18.0	15.4	13.3	11.8	10.5	9.5	8.7	8.0	
τ		0.6	0.9	1.4	2.0	2.4	2.4	2.1	1.2	1.1	1.4	2.0	2.4	
ω		0.05	0.13	0.25	0.29	0.31	0.29	0.26	0.23	0.43	0.65	0.75	0.79	
g		0.03	0.07	0.14	0.23	0.34	0.41	0.48	0.55	0.60	0.64	0.69	0.72	
I(%)	1	3	7	10	11	10	11	12	8	7	5	4	3	8

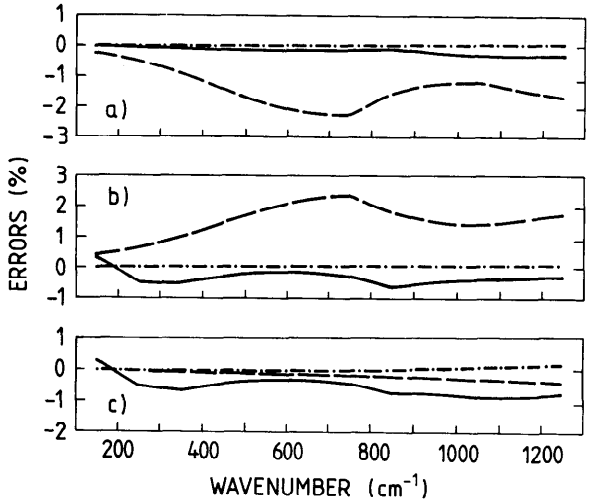

Fig. 1. Relative errors of (a) upward flux at top, (b) downward flux at bottom, and (c) flux divergence in layer for an inversion cloudy profile: (——) for four-stream linear approximation; (·) for 16-stream linear approximation; (– – –) for 16-stream isothermal approximation.

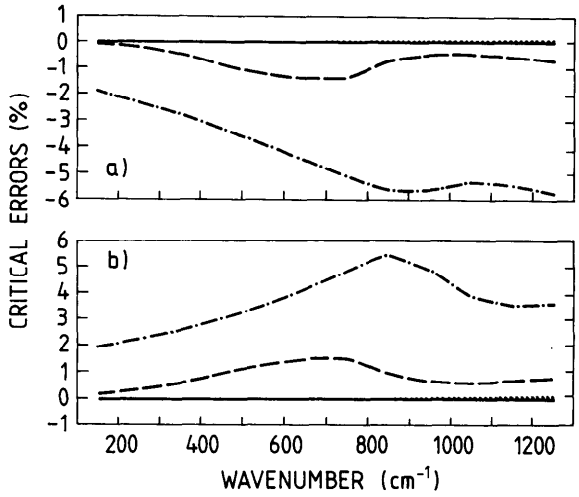

Fig. 2. Critical errors of (a) upward intensity at top and (b) downward intensity at bottom for an inversion cloudy profile: (——) for minimum; (· · ·) for maximum errors of linear approximation; (– – –) for minimum; (– · –) for maximum errors of isothermal approximation.

computing time is spent on radiative transfer computations, since they must be performed many times over the time and space domains.

4. DESCRIPTION OF RADIATION MODEL

4.1. Molecular absorption/emission

More than 99% of the Earth's atmosphere is composed of nitrogen and oxygen gases. Because these two gases consist of diatomic molecules, they do not absorb radiant energy for wavelengths longer than the u.v. portion of the spectrum, except for a narrow absorption band around 0.76 μm for O_2. In clear-sky atmospheres, they are predominantly responsible for atmospheric scattering of radiation (Rayleigh scattering), which is of relatively greatest importance compared to absorption at visible and near u.v. wavelengths. The atmospheric (or greenhouse) effect which provides a habitable environment for life on Earth is due to the absorption/emission of terrestrial radiation by trace gases ($<1\%$ of the air): mainly water vapor (H_2O), carbon dioxide (CO_2), and ozone (O_3). The combined effect of other minor trace gases (e.g., N_2O, CH_4, CFCs) also contribute to the greenhouse effect,[15–17] but will not be considered in this study.

Figure 3(a), modified from Coulson[18] and Liou,[19] shows an overall picture of the clear-sky radiation. For convenience it has been customary to separate solar and terrestrial radiation at 4 μm because of the negligible amounts of energy existing on either side of 4 μm for each relative to the other. It should be kept in mind, however, that such simplification is inadequate for applications to remote sensing if the reflected solar radiation received by the sensor is comparable to the terrestrial thermal emission [e.g., channel 3 (3.55–3.95 μm) of TIROS-N/NOAA Advanced Very High Resolution Radiometer].

For solar radiation, the outer curve in Fig. 3(a) was observed at the top of the atmosphere while the inner curve was observed at sea level. The shaded area is due to absorption by gases (H_2O, CO_2, and O_3) and the area between the outer curve and the shaded area is caused by scattering. For terrestrial radiation (note that the vertical scale is different), the emission spectrum was observed by satellite interferometer from space. The surface was emitting at a temperature of about 300 K. The two dips in the emission spectrum were caused by the re-emission of CO_2 and O_2 at their atmospheric temperatures (about 220 and 260 K, respectively), and radiation emitted from the surface was completely absorbed in those two bands. Water vapor and continuum absorption/emission cover large portions of the spectrum and are dominant in the moist portion of the atmosphere consisting primarily of the middle and lower troposphere.

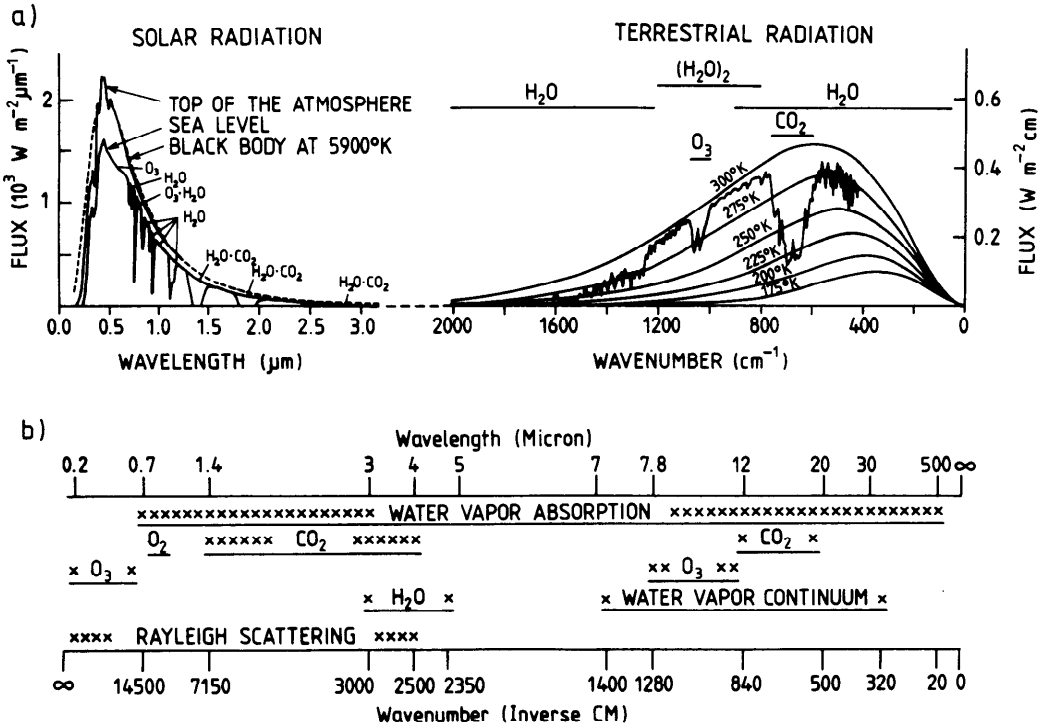

Fig. 3. Spectral distribution of (a) gaseous scattering and absorption/emission for two clear-sky observations (modified from Coulson[18] and Liou[19]) and (b) for exponential-sum fitting of transmission for gaseous absorption/emission.

Due to the small amount of energy involved in transitions from one quantum state to another, the gaseous rotational/vibrational absorption spectra consist essentially of complex, closely spaced line structures. The necessary spectral line parameters (e.g., frequency at line center, intensity, half-width) have been compiled and reported by McClathchey et al[20] and continuously updated since then to include some 348,000 lines (Rothman et al[21]). The difficulty involved in incorporating either fine line structure (e.g., resulting in time-consuming computations) or broad band measurement absorption data (due to large atmospheric temperature and pressure variations) into multiple scattering radiation models has been discussed by several investigators.[22–25] Therefore, parameterization of gaseous absorption over a spectral region containing many lines is needed for computational efficiency when absorption is included in a multiple scattering scheme. For this purpose, two methods, named exponential-sum fitting of transmissions (ESFT) and photon path-length distributions (PPLD), have been established.

The ESFT method approximates the transmission function of a given spectral region by a finite sum of M exponential terms as follows:[26–28]

$$\tilde{T}(u) \sum_{i=1}^{M} w_i \exp(-b_i u) \quad \text{and} \quad \sum_{i=1}^{M} w_i = 1. \tag{5}$$

Here, $\tilde{T}$ denotes the band transmission function and u is the equivalent absorber amount. The b_i are the equivalent absorption coefficients and the w_i are associated weights ($b_i \geqslant 0$, $w_i > 0$). On the other hand, the PPLD method introduces a photon path-length distribution function $\epsilon(y)$ (y, the path length) into the transfer equation.[29,30] This function can be determined by, for example, the Monte Carlo technique. Although these two methods have been shown to be equivalent,[31] the ESFT method has three advantages: (1) the $b_i u$ behave like monochromatic optical depths which can easily be incorporated into the multiple scattering scheme; (2) in view of the observed multiplication property of the transmission,[32] the overlap of absorbing gases can be treated easily, although at the expense of an increased number of pseudo-gray absorption coefficients; (3) a unified treatment of shortwave and longwave radiation is achieved. Therefore, the ESFT method is adopted for the

present study. In essence, the main virtue of the ESFT method is to reduce the non-gray radiative transfer problem involving integration over a finite spectral interval (for which Beer's law does not apply) to a series of monochromatic problems. A unified treatment of scattering and absorption/emission in both the shortwave and longwave parts of the spectrum has previously been used by others.[10, 33]

Figure 3(b) shows the spectral regions in which the four gases, considered in this study, absorb radiant energy. The ESFT method is used to deal with each gas in the wavelength intervals shown. Water vapor absorption is important for almost the enitre spectrum except for wavelengths shorter than 0.7 μm. Carbon dioxide has absorption bands in the near-i.r. (around 1.4–5 μm) as well as in the i.r. (centered at 15 μm). Ozone absorbs strongly in the u.v. (Hartley and Huggins bands), weakly in the visible (Chappuis band) and has a strong absorption band in the i.r. centered at 9.6 μm. A narrow absorption band due to oxygen molecules is located at 0.76 μm. Since solar radiation of wavelengths shorter than 0.2 μm is absorbed completely by atomic and molecular oxygen and nitrogen gases before reaching the stratosphere, the spectral region appropriate for the present study is from 0.2 to 500 μm. Therefore, each set of b_i and w_i for gaseous absorption by H_2O, CO_2, O_3 and O_2 is obtained by fitting the LOWTRAN-6 (LOW-resolution TRANsmission, version 6) transmission functions[34] with 20 cm^{-1} spectral intervals. LOWTRAN also accounts for the continuum absorption by a foreign-broadening band from 3.3 to 4.2 μm and a self-broadening band from 7 to 31 μm. Two different sets of ESFT coefficients have kindly been provided to us by Wiscombe (1985, personal communication) and by Slingo and Schrecker.[24] In general, the former set contains regular spectral intervals (20 cm^{-1} in the longwave and larger wavenumber intervals in the shortwave) over the entire spectrum and with overlapping gaseous absorption. The latter set treats only shortwave radiation for O_3 and H_2O absorption in irregular spectral intervals and without overlapping.

Empirical scaling of absorber amounts (u_0) is needed to account for the pressure and temperature dependence. Thus, the effective absorber amount (u) is obtained as follows:

$$u(z) = u_0(z)\left\{\frac{p(z)}{p(0)}\left[\frac{T(0)}{T(z)}\right]^{1/2}\right\}^n, \tag{6}$$

where $p(0) = 1013.25$ mbar; $T(0) = 273.15$ K; and the parameter n is determined empirically to be 0.9 for H_2O, 0.75 for the uniformly mixed gases (CO_2 and O_2), and 0.4 for ozone.[34] We note that the exponent n in Eq. (6) stays constant over the whole spectrum and can not account for the variation with wavenumber of the pressure and temperature dependence of the absorption for various line regimes in different parts of the spectrum. Thus, this one-parameter scaling of absorber amounts, required by LOWTRAN, is generally expected to be less accurate than the two-parameter Curtis–Godson approximation to deal with the pressure and temperature variations along the optical paths.[32]

4.2. Molecular scattering

Rayleigh scattering is important only in the spectral region from 0.2 to 0.4 μm, due to the dependence of scattered radiation on λ^{-4} (λ, monochromatic wavelength). Penndorf's[35] formula for Rayleigh's volume extinction coefficient (β_R, m^{-1}) has been widely adopted (cf. e.g., Refs. 24 and 34) and is given as follows:

$$\beta_R(z) = [0.9793(n_a^2 - 1)^2 p(z)]/[\lambda^4 T(z)], \tag{7}$$

where n_a denotes the refractive index of air and temperature and pressure dependence is also taken into account. Recently, Nicolet[36] showed that the Rayleigh scattering cross sections (σ_R, cm^2) can be expressed by a simple empirical formula for wavelengths from 0.2 to 1 μm, viz.

$$\sigma_R = 4.02 \times 10^{-28}/\lambda^{4+f} \quad (\lambda \text{ in } \mu\text{m}), \tag{8}$$

where $f = 0.389\lambda + 0.09426/\lambda - 0.3228$ for $\lambda < 0.55$ μm; and $f = 0.04$ for $\lambda > 0.55$ μm. We provide a comparison between these two different Rayleigh scattering parameterization schemes (Sec. 5, Table 9).

For testing and validation purposes, we use the five profiles of the McClathey atmospheres appropriate for tropical, midlatitude summer and winter, and subarctic summer and winter

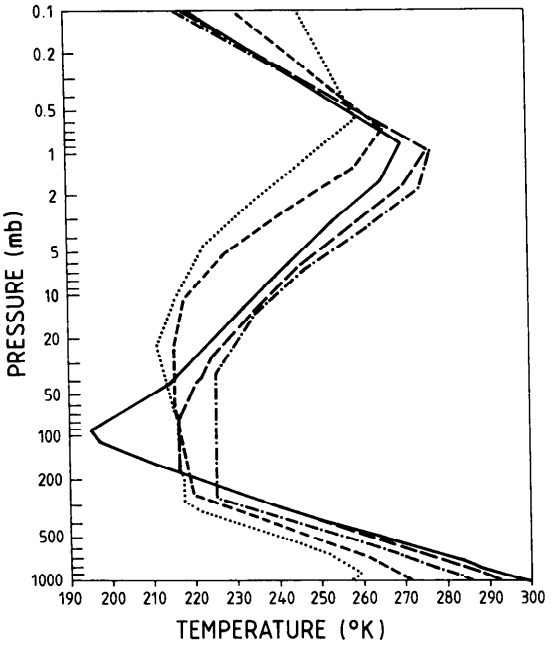

Fig. 4. Temperature profiles for five McClatchey atmospheres: (——) tropical; (— — —) midlatitude summer; (– – –) midlatitude winter; (– · –) subarctic summer; (· · ·) subarctic winter.

Table 5. Comparisons of fluxes computed by different methods for CO_2, O_3, and H_2O (without continuum) absorption (0–2600 cm^{-1}) in a midlatitude summer atmosphere. $F^+(\tau_N)$ denotes upward flux at bottom; $F^-(\tau_N)$, downward flux at bottom; $F^+(0)$, upward flux at top; ΔF_{sfc} and F_{atm} net flux loss of surface and entire atmosphere, respectively (all in dimension of W m^{-2}).

Method	$F^+(\tau_N)$	$F^-(\tau_N)$	ΔF_{sfc}	$F^+(0)$	ΔF_{atm}
GFDL L-BY-L	423.15	303.46	119.69	294.42	174.73
LMD L-BY-L	423.09	302.80	120.29	293.69	173.40
ESFT†20cm^{-1}	423.13	300.22	122.91	288.22	165.31
ESFT‡20cm^{-1}	423.13	303.83	119.30	282.87	163.57

†as shown in Fig. 1b; ‡as in [1] except including O_3 absorption in 580-840cm^{-1}, 1600-2320cm^{-1} and CO_2 absorption in 900-1660cm^{-1}, 1820-2500cm^{-1}.

conditions.[37] Temperature and pressure profiles for these five atmospheres, each having 33-level vertical resolution, are shown in Fig. 4. The CO_2 concentration is assumed to be 330 ppmv with a constant mixing ratio. To compare our results with others in the shortwave region, we adopt the total solar irradiance at the top of the atmosphere and its spectral energy distribution from the works of Thekaekara and Drummond[38] and of Labs and Neckel.[39] These two sets of coefficients are slightly different in both solar constant and spectral distribution.

5. RESULTS AND COMPARISONS

5.1. Longwave radiation: 4–500 μm (or 20–2500 cm^{-1})

The i.r. region can be roughly divided into three major bands and three overlapping bands. The three major bands are the water vapor rotational band (20–840 cm^{-1}), the window region (840–1400 cm^{-1}), and the water vapor vibrational (1400–2500 cm^{-1}). Ozone absorption (580–1280 cm^{-1}) partially overlaps with both the H_2O rotational band and the window region. Carbon dioxide absorption (540–800 cm^{-1}) overlaps entirely with the H_2O rotational band. Water vapor continuum absorption (320–1400 cm^{-1}) overlaps partially with the H_2O rotational band and entirely with the window region.

Comparisons with other model results are presented below. First we note that the ESFT coefficients based on LOWTRAN-6 provided to us by Dr. Wiscombe are basically consistent with the line-by-line database[21] (except for two water vapor bands in the near-i.r.). This fact makes the following comparisons more meaningful.

Results of line-by-line methods[40] adopted in this study as a benchmark are from the Geophysical Fluid Dynamics Laboratory (GFDL) and the Laboratoire de Météorologie Dynamique (LMD). The GFDL and the LMD models are different in vertical resolution (51 and 40 levels, respectively) and in treatment of spectral line parameters (i.e., spectroscopic data, line cutoff). In Table 5, we compare fluxes as computed by the GFDL, the LMD and two present ESFTs for gaseous absorption in a midlatitude summer atmosphere. The difference between the two ESFTs is the wavenumber range of overlapping gases. The spectral distribution of ESFT1 is identical to that shown in Fig. 3(b). Additional O_3 absorption in wavenumber intervals of 580–840 and 1600–2320 cm^{-1}, and CO_2 absorption of 900–1600 and 1820–2500 cm^{-1} are included in the spectral

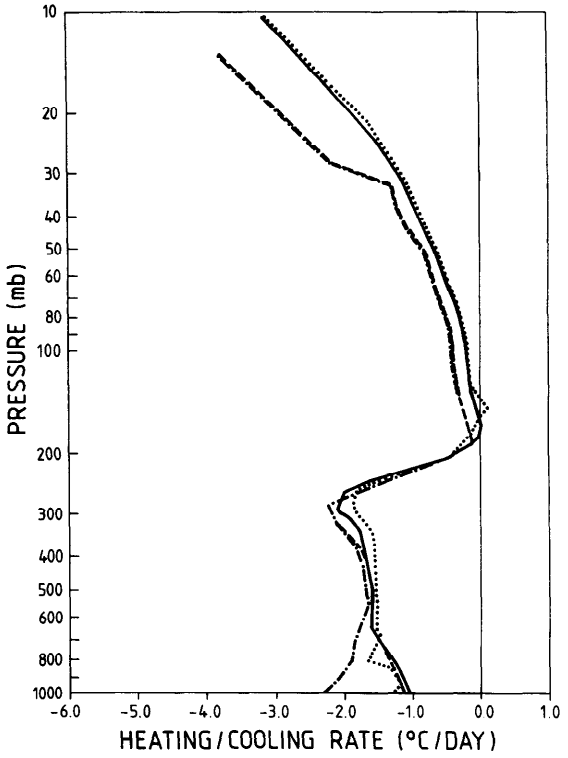

Fig. 5. Heating/cooling rates of carbon dioxide, ozone, water vapor (with an without continuum) absorption for midlatitude summer atmosphere; (——) GFDL line-by-line; (· · ·) LMD line-by-line; (– – –) ESFT 20 cm^{-1} without continuum; (– · –) ESFT 20 cm^{-1} with continuum.

Table 6. Comparisons of fluxes computed by different methods for water vapor absorption (0–580 and 1220–2020 cm^{-1}) and CO_2 absorption (540–800 cm^{-1}) (values in parentheses are for double CO_2 amount) in tropical and subarctic winter atmospheres. (Notation as in Table 5.)

(a) Tropical Atmosphere

Method	Gas	$F^+(\iota_N)$	$F^-(\iota_N)$	$F^+(0)$	F_{atm}
Line-By-Line	H_2O	221.29	211.88	133.40	123.99
ESFT 20cm^{-1}	H_2O	221.29	208.66	137.58	124.95
Line-By-Line	CO_2	120.76	78.45 (84.98)	75.11 (70.88)	32.80 (35.10)
ESFT 20cm^{-1}	CO_2	120.76	77.29 (83.18)	71.75 (68.16)	28.28 (30.58)

(b) Subarctic Winter

Method	Gas	$F^+(\iota_N)$	$F^-(\iota_N)$	$F^+(0)$	ΔF_{atm}
Line-By-Line	H_2O	130.85	99.45	106.85	75.45
ESFT 20cm^{-1}	H_2O	130.85	106.19	108.22	83.56
Line-By-Line	CO_2	69.63	41.75 (45.22)	50.94 (49.16)	23.06 (24.75)
ESFT 20cm^{-1}	CO_2	69.63	46.40 (49.69)	49.30 (47.68)	26.07 (27.74)

distribution of ESFT2. Very good agreement is found for surface fluxes to within 1–3 W-m^{-2} for the three major gaseous absorption species (CO_2, O_3, and H_2O without continuum). A reduction of absorbing gases (ESFT1 vs ESFT2 in Table 5) further cooled the surface by about 3 W-m^{-2} and cooled the atmosphere by about 2 W-m^{-2} which in turn increased energy loss at the top by about 5 W-m^{-2}. The major difference in the upward flux at the top (5–11 W-m^{-2}) is essentially due to CO_2 emission.

Heating/cooling profiles of CO_2, O_3, and H_2O (with and without continuum) absorption for the midlatitude summer atmosphere are shown in Fig. 5. The inclusion of continuum absorption is important when considering the lower troposphere because of the high vapor partial pressure, especially near the surface. Generally, very good agreement (no continuum absorption) is achieved between the present ESFT and the GFDL line-by-line methods to within 0.2°C per day below the 30 mbar level. However, in spite of the excellent flux agreement between the GFDL and the LMD methods (to within 1 W-m^{-2} as shown in Table 5), their cooling rates show a maximum discrepancy up to 0.3°C per day in the troposphere. The cause of this discrepancy needs to be studied more carefully, since atmospheric thermal stability is determined by the detailed shape of the heating/cooling profile. This suggests that models giving correct bulk radiative quantities may give inadequate heating/cooling rates, due to possible compensating errors. Thus, model validation should include detailed verification of the net flux as a function of altitude in addition to the values at the boundaries of the atmosphere.

Table 6 shows fluxes computed at the top and the bottom of the tropical and subarctic winter atmospheres for water vapor absorption (0–580 and 1200–2020 cm^{-1}) and carbon dioxide absorption (540–800 cm^{-1}). Values for the line-by-line method are taken from Chou and Arking[22] for H_2O and from Chou and Peng[41] for CO_2. Fluxes obtained by line-by-line computations for the H_2O and CO_2 molecules, based on the line parameters compiled by McClatchey et al,[20] may serve as benchmarks. The line shape is assumed to be the Voigt profile, cut off at 10 cm^{-1} from the line center.[22] Instead of using 33 levels, Chou and Arking interpolated the McClatchey atmospheres to

55 levels and assumed a constant temperature across each layer. The top of the atmosphere is set at 1 mbar and the surface, assumed to be blackbody, is at 1000 mbar.

We find good agreement between line-by-line computations and present ESFT 20 cm^{-1} results in the tropical atmosphere for water vapor absorption. The difference in flux divergence ranges from 1 W-m^{-2} in tropical (TRO) to 8 W-m^{-2} in subarctic winter (SAW) atmospheres, which we attribute to the large discrepancy in the downward fluxes at the surface. Two possible causes may account for this large discrepancy in SAW. First, the water vapor is highly concentrated in the lower troposphere. Different interpolation schemes (55 levels in line-by-line and 33 levels in ESFT) of the absorber amount will affect the H_2O absorption in the wing region. Second, the surface inversion in SAW, in contrast to TRO, could be the major cause of the discrepancy in the downward flux, due to the temperature and pressure scaling used in ESFT. Figure 6 shows the heating/cooling profiles of water vapor absorption for TRO and SAW. Results from the line-by-line and the present ESFT methods agree generally within 0.1–0.2°C per day, except for the large difference in the surface inversion region for SAW, which is consistent with Table 6.

The differences in CO_2 absorption are around 3–4 W-m^{-2}. The largest discrepancy occurs in the upward flux for the TRO atmosphere and in the downward flux for the SAW atmosphere. Doubling of the absorber amounts does not alter discrepancies of the net flux loss for the entire atmosphere, but affects the redistribution instead. Heating/cooling rates due to CO_2 absorption for TRO and SAW are shown in Fig. 7. Very good agreement between the two methods is found below the lower stratospheres of TRO and SAW. However, the large discrepancies (up to 2°C per day) of cooling rates above 40 mbar are partially due to the lower spatial resolution used in ESFT. To improve the vertical resolution, we introduced three more sublayers between each original layer above the 40 mbar into the TRO atmosphere. Better agreement is found while the discrepancy in the fluxes shown in Table 6 for TRO remains the same. This shows that the heating/cooling rates are sensitive to the vertical resolution, especially at high altitudes where pressure varies rapidly with the height and the pressure scaling factor becomes dominant. The remaining discrepancy above 40 mbar may be due to the pressure scaling adopted in Eq. (6), but this remains to be investigated.

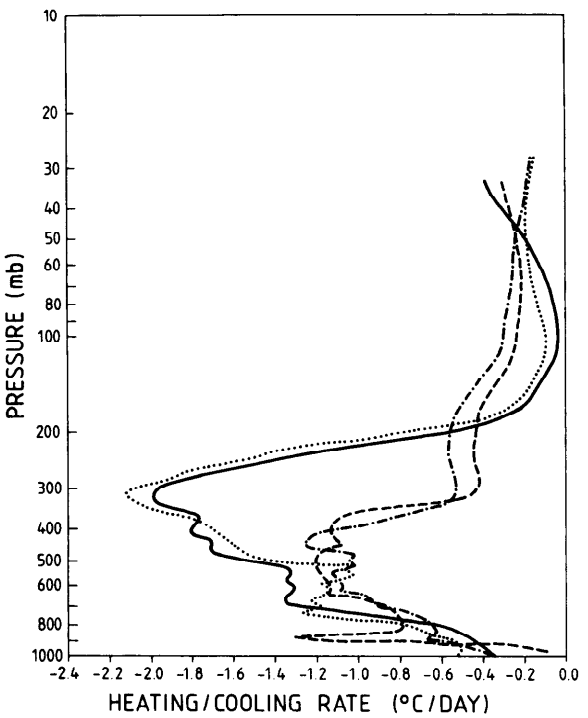

Fig. 6. Heating/cooling rates of water vapor absorption for tropical (——) line-by-line; (· · ·) ESFT 20 cm^{-1} and subarctic winter (– – –) line-by-line; (– · –) ESFT 20 cm^{-1} atmospheres.

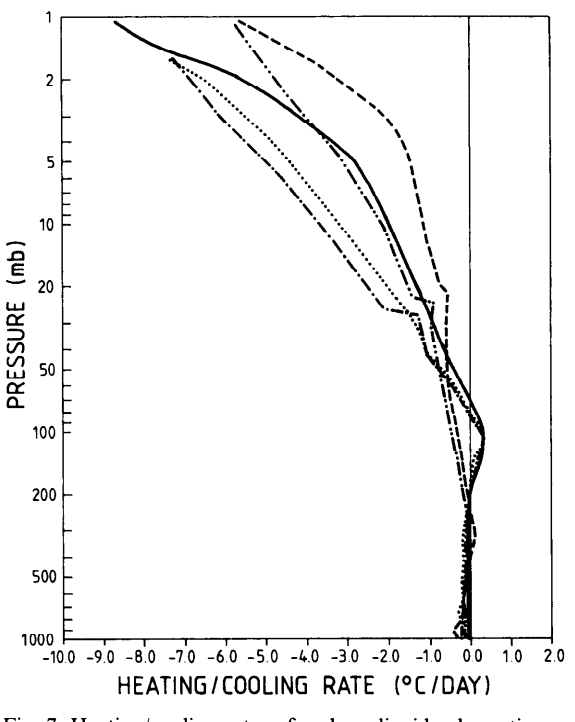

Fig. 7. Heating/cooling rates of carbon dioxide absorption for tropical (——) line-by-line; (– · –) ESFT 20 cm^{-1}; (· · ·) ESFT 20 cm^{-1} with high vertical resolution and subarctic winter (– – –) line-by-line; (– · · –) ESFT 20 cm^{-1} atmospheres.

Table 7. Comparisons of fluxes and heating/cooling rates computed by different methods for water vapor absorption with 60° zenith angle and zero surface albedo in tropical and midlatitude winter atmospheres. (Notation as in Table 5, except ΔF_{atm} for net flux gain of entire atmosphere and HCR for heating/cooling rate [°C/day].)

(a) Tropical Atmosphere

Spectral (cm^{-1})	Method	ΔF_{atm}	HCR
2600-12040	Line-By-Line	105.60	0.892
2600-12040	Far-Wing Scaling	104.70	0.884
2600-12040	ESFT Narrow-Band	98.55	0.831
2500-12820	ESFT Narrow-Band	101.07	0.852
2500-12820	ESFT Broad-Band	102.00	0.860

(b) Midlatitude Winter

Spectral (cm^{-1})	Method	ΔF_{atm}	HCR
2600-12040	Line-By-Line	71.20	0.601
2600-12040	Far-Wing Scaling	72.70	0.615
2600-12040	ESFT Narrow-Band	72.55	0.608
2500-12820	ESFT Narrow-Band	73.61	0.617
2500-12820	ESFT Broad-Band	74.52	0.626

5.2. Shortwave radiation: 0.2–4.0 μm (or 2500–50,000 cm^{-1})

In the spectral region of 2.5–4.0 μm, the ESFT coefficients (provided by Wiscombe) pertains to 20 cm^{-1} intervals. However, in the region of 1.0–2.5 μm the spectral resolution is < 100 cm^{-1}, which is still in the category of narrow-band models (NBM).[40] On the other hand, broad-band models (BBM) contain spectral widths larger than 100 cm^{-1} (e.g., the ESFT coefficients of O_3 and H_2O provided by Slingo and Schrecker[24]). The present ESFT-NBM treats the gaseous absorption of H_2O, CO_2, O_2 and O_3, while the BBM is an extension of the ESFT coefficients provided by Slingo and Schrecker[24] to include the additional absorbing gases O_2 and CO_2.

Table 7 shows net fluxes gained (difference in net flux between two boundaries) and heating/cooling rates of the entire atmosphere for various methods of dealing with water vapor absorption in the tropical and midlatitude winter atmospheres, where the zenith angle is 60° and the surface albedo is zero. Values for the line-by-line and far-wing scaling computations of Chou and Arking[23] are shown for comparison. The line-by-line method is essentially the same as the one described previously. The far-wing scaling method is based on the k-distribution function,[42] where the spectral interval is set to be 40 cm^{-1}. Comparisons for the spectral interval of 2600–12,040 cm^{-1} were done by using Labs and Neckel's solar spectrum data set and for 2500–12,820 cm^{-1} by using Thekaekara and Drummond's. Ignoring the slightly different spectral ranges utilized by us and Chou and Arking, systematic discrepancies are observed. Thus, our broad-band values are consistently larger than those of the narrow-band ESFT by about 1 W-m^{-2} for both the tropical and the midlatitude winter atmospheres. However, Chou and Arking obtain larger values by the far-wing scaling than by the line-by-line for the midlatitude winter atmosphere, but smaller values for the tropical atmosphere even though their computational setup is identical. When our ESFT-NBM is applied in the same spectral region as Chou and Arking's line-by-line model, good agreement is achieved for the midlatitude winter but only fair for the tropical atmosphere (cf. Table 7). This discrepancy could be due to the use of different vertical resolution by us and Chou and Arking.

Heating/cooling rate profiles for the tropical and midlatitude winter atmospheres are shown in Fig. 8. Very good agreement between the ESFT-NMB and the ESFT-BBM heating profiles is obtained, as expected from Table 7, except around the tropopauses. The major difference of heating rates (maximum of 0.3°C per day) between the line-by-line and the ESFT for the tropical atmosphere is observed below 600 mbar, the location of the major concentration of H_2O. The sudden jump around the tropopause of the heating rate computed by the line-by-line method for the midlatitude winter atmosphere is quite strange, and could be caused by the layering structure.

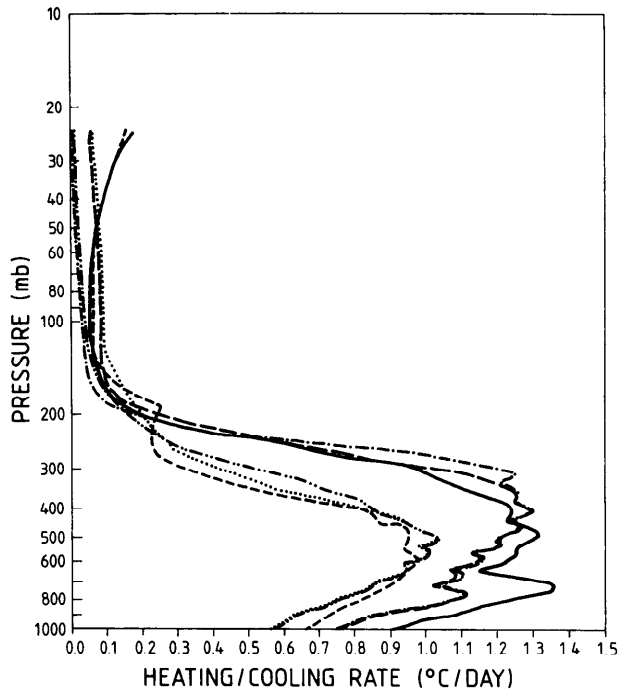

Fig. 8. Solar heating rates of water vapor absorption for tropical (——) line-by-line; (— — —) narrow-band; (— · —) broad-band and midlatitude summer (– – –) line-by-line; (· · ·) narrow-band; (– · · –) broad-band atmospheres.

Because of the limited studies available in the open literature, further comparisons between the ESFT and line-by-line methods are difficult to make for other gases such as for O_2 absorption. We therefore, provide intercomparisons of the ESFT models for O_3 absorption and other gases. Table 8 shows comparisons of fluxes for O_3 absorption with a 30° solar zenith angle and a zero surface albedo in the subarctic summer atmosphere. Slingo and Schrecker[24] used the empirical constant 0.0 instead of 0.4 in LOWTRAN scaling of the ozone absorber amount [Eq. (6)], arguing that the value 0.4 has not been validated under conditions of multiple scattering. We therefore, present test computations with (i.e, factor 0.4) and without (i.e., factor 0.0) scaling in Table 8.

The narrow-band-S (NBS) model contains two weak O_3 absorption bands (3.3 and 3.6 μm) in the near-i.r. region and strong absorption bands at wavelengths shorter than 0.7 μm. On the other hand, the narrow-band-V (NBV) model eliminates the two weak absorption bands and so does the

Table 8. Comparisons of fluxes computed by different methods for O_3 absorption with 30° zenith angle and zero surface albedo in subarctic summer atmosphere. (Notation as in Table 7, except ΔF_{tro} for net flux gain above tropopause, S for O_3 absorption in entire shortwave region; V for O_3 absorption outside near-i.r. region.)

(a) O_3 absorber amount without scaling ($n = 0.0$)

Method	$F^{-}(0)$	$F^{-}(\tau_N)$	ΔF_{atm}	ΔF_{tro}
Narrow-Band-S	645.11	616.42	28.69	27.31
Narrow-Band-V	645.11	616.95	28.16	26.83
Broad-Band-V	645.11	615.58	29.53	28.22

(b) O_3 absorber amount with scaling ($n = 0.4$)

Method	$F^{-}(0)$	$F^{-}(\tau_N)$	ΔF_{atm}	ΔF_{tro}
Narrow-Band-S	645.11	626.30	18.81	17.09
Narrow-Band-V	645.11	626.50	18.61	16.94
Broad-Band-V	645.11	625.76	19.35	17.77

Table 9. Comparisons of flux computations for two different Rayleigh scattering parameterizations for various zenith angles and surface albedo values in a subarctic summer atmosphere. (Notation as in Table 8.)

(a) Surface albedo (0.0)

Zenith	$F^-(\tau_N)$	$F^+(0)$	ΔF_{atm}		$F^-(\tau_N)$	$F^+(0)$	ΔF_{atm}
30°	700.29	51.88	59.00		700.80	51.37	59.00
60°	378.89	46.12	43.31		379.31	45.70	43.31
75°	175.10	37.35	29.97		175.38	37.05	29.99

(b) Surface albedo (0.8)

Zenith	$F^-(\tau_N)$	$F^+(0)$	ΔF_{atm}		$F^-(\tau_N)$	$F^+(0)$	ΔF_{atm}
30°	762.52	576.67	81.99		762.53	576.66	81.99
60°	410.96	331.80	54.34		411.13	331.75	54.34
75°	188.97	170.23	34.40		189.15	170.17	34.42

broad-band-V (BBV) model but with wider spectral intervals. Additional absorption by the entire atmosphere due to the weak bands ranges from 0.2 to 0.5 W-m^{-2} (Table 8 ΔF_{atm} of NBS vs NBV) and takes place above the tropopause (Table 8 ΔF_{tro}). Thus, for most applications, the weak band absorption could be eliminated without making serious errors. The BBV vs NBV systematically overestimates the ozone absorption for the entire atmosphere by about 1 W-m^{-2}, which is consistent with the H_2O absorption in Table 7 (ESFT-BBM vs NBM). This could be due to the fact that the solar radiation is taken to be constant over the spectral intervals, if we assume the same accuracy for the fitting of transmission functions in the narrow- and broad-band models.

Pressure and temperature scaling [$n = 0.4$ of Eq. (6)] substantially decreases the absorber amount in the upper atmosphere where the major absorption of ozone occurs. This fact causes absorption by the entire atmosphere to be reduced by about 35%. The reduction is due mainly to the weak absorption of ozone in the visible region because the strong ozone absorption in the u.v. becomes easily saturated whether scaling is used or not. But the major heating for the scaled ozone profile becomes weaker and shifts downward, because radiation penetrates deeper due to the diluted effective absorber amount. Further studies are needed to assess the necessity and accuracy of this scaling. However, since near u.v. ozone absorption bands show continuum features, scaling may not be necessary in this spectral range.

Rayleigh scattering is important in the shortwave region. Table 9 examines two different parameterizations of Rayleigh scattering optical parameters for flux computations for various zenith angles and surface albedo values in a subarctic summer atmosphere. Excellent agreement is found between results using Penndorf's [Eq. (7)] and Nicolet's [Eq. (8)] empirical formulas in the spectral range 0.25–1.0 μm, where absorption by O_3, O_2 and H_2O occurs. Absorption by the entire atmosphere is almost identical and the difference between the upward fluxes at the top and the downward fluxes at the bottom is within 0.5 W-m^{-2}.

Absorptions by O_2 and CO_2 in the near-i.r. region is also examined for the scattering atmosphere, as shown in Table 10. Because the CO_2 absorption is overlapping with the strong absorption of H_2O, inclusion of CO_2 only increases atmospheric absorption by about 4.3 W-m^{-2} and cools the surface by about 3.3 W-m^{-2} in the subarctic summer atmosphere. The effect of O_2 absorption has the same order of magnitude as does the CO_2 absorption.

6. SUMMARY AND CONCLUSIONS

We have verified a reliable and efficient discrete-ordinate-method for radiative transfer in vertically inhomogeneous, non-isothermal atmospheres. The linear-in-optical-depth approximation to the Planck function is used to obtain accurate solutions for thermal emission computations. Numerical results demonstrate that this approximation significantly improves computing efficiency while still maintaining adequate accuracy.

We have used this method to construct a radiation model applicable for scattering and absorbing/emitting layered media. To verify our model we have made comparisons with line-by-line calculations for the McClatchey atmospheres. The line-by-line methods can be very accurate, but

Table 10. Comparisons of flux computatons for gaseoius absorption with 30° zenith angle and 0.8 surface albedo in a subarctic summer atmosphere. (Notation as in Table 8.)

(a) gaseous absorption + Rayleigh scattering in 1500-12820cm^{-1}

Gases	$F^{-}(0)$	$F^{-}(\tau_N)$	ΔF_{atm}	ΔF_{tro}
H_2O+CO_2	528.09	386.72	165.18	7.63
H_2O only	528.09	390.03	160.89	5.64

(b) gaseous absorption + Rayleigh scattering in 12820-4000cm^{-1}

Gases	$F^{-}(0)$	$F^{-}(\tau_N)$	ΔF_{atm}	ΔF_{tro}
$O_3+H_2O+O_2$	634.41	605.47	54.35	43.38
O_3+H_2O	634.41	609.54	49.21	41.85

they are very time-consuming. The AFGL (Air Force Geophysics Laboratory) compilation contains over 348,000 lines from 0 to 17,900 cm^{-1} (Rothman et al[21]). Therefore, when applying line-by-line methods, the transfer equation has to be solved over 348,000 times. Practically, this is suitable for validating models only. The present ESFT2 model implies about 16,000 monochromatic calculations from 20 to 50,000 cm^{-1} for H_2O, CO_2 and O_3 gaseous absorption, of which about 9800 are in the i.r. region. This reduction from line-by-line to ESFT narrow band for fast computation in the i.r. region introduces errors in flux computations ranging from 1 to 7 $W\text{-}m^{-2}$ in the five McClatchey atmospheres. Elimination of detailed overlapping gaseous absorption in the i.r. (i.e., ESFT1 model) reduces our computational burden to only 2800 monochromatic problems. The elimination of this overlapping introduces errors in flux computations ranging from 1 to 5 $W\text{-}m^{-2}$ compared with the ESFT2 narrow band results.

In the shortwave region, the broad-band ESFT is acceptable for applications which can tolerate errors in fluxes to within a few $W\text{-}m^{-2}$. Substantial amounts of computer time are saved due to the reduction of terms from 6200 in the narrow-band to 410 in the broad-band ESFT method which only create errors in flux computations to within 1 $W\text{-}m^{-2}$. When O_2 and CO_2 absorption is neglected, the number of terms can be further reduced to 141, as in the model of Slingo and Schrecker.[24] The error introduced by eliminating O_2 or CO_2 absorption is equally important and ranges from 3 to 4 $W\text{-}m^{-2}$. The Rayleigh scattering parameterizations of Penndorf and Nicolet perform equally well in the presence of molecular absorption.

Among the existing methods of treating molecular absorption, the ESFT method is a very convenient one for incorporating gaseous absorption into multiple scattering models.[25] The major discrepancy in flux computations compared with the line-by-line results come from the empirical temperature and pressure scaling, especially in the upper atmosphere. Further studies are needed to assess the necessity and accuracy of the empirical scaling. Thus, our results indicate that while the ESFT method is useful for tropospheric applications, its validity in the stratosphere is questionable. We also find that in spite of good agreement between fluxes (at the top and bottom boundaries) computed by different methods, the heating/cooling rate profiles may differ substantially due to compensating errors. Since atmospheric thermal stability is determined by the detailed shape of the heating/cooling profile, this discrepancy suggests that model validation should include detailed verification of the net flux as a function of altitude in addition to the values at both boundaries.

Acknowledgements—We are very pleased to thank A. Slingo and W. Wiscombe for providing their ESFT coefficients. This study was supported by the National Science Foundation through Grants DPP 84-06093 and DPP 86-18706.

REFERENCES

1. D. F. Heath, A. J. Krueger, A. A. Roeder, and B. O. Henderson, *Opt. Engng* **14,** 323 (1975).
2. K. Stamnes, S. C. Tsay, W. Wiscombe, and K. Jayaweera, *Appl. Opt.* **27,** 2502 (1988).
3. S. C. Tsay, K. Stamnes, and K. Jayaweera, *J. Atmos. Sci.* **46,** 1002 (1989).
4. S. Chandrasekhar, *Radiative Transfer*, Dover, New York, NY (1960).
5. K. Stamnes, *Rev. Geophys.* **24,** 299 (1986).
6. W. J. Wiscombe, *JQSRT* **16,** 637 (1976).

7. K. Schwarzschild, in *Selected Papers on the Transfer of Radiation*, M. Menzel ed., Dover, New York, NY (1906).
8. J. F. Geleyn and A. Hollingworth, *Contr. Atmos. Phys.* **52,** 1 (1979).
9. A. Hense, M. Kerschgens, and E. Raschke, *Q. Jl R. Met. Soc.* **108,** 281 (1982).
10. W. J. Wiscombe, R. M. Welch, and W. D. Hall, *J. Atmos. Sci.* **41,** 1336 (1984).
11. W. J. Wiscombe, *JQSRT* **16,** 637 (1976).
12. *Radiative Transfer in Scattering and Absorbing Atmospheres: Standard Computational Procedures*, J. Lenoble ed., Deepak, Hampton, VA (1985).
13. S. C. Tsay and K. Jayaweera, *J. Clim. Appl. Met.* **23,** 584 (1984).
14. G. L. Stephens, "Optical Properties of Eight Water Cloud Types", Tech. Pap. **36,** CSIRO Aust. Div. Atmos. Phys., Melbourne, Australia (1979).
15. *WMO Global Ozone Research and Monitoring Project*, WMO Report No. 14, V. Ramanathan and R. D. Bojkov eds., Geneva (1982).
16. W. J. Wiscombe, *Rev. Geophys. Space Phys.* **21,** 997 (1983).
17. J. Morcrette and Y. Fouquart, *Q. Jl R. Met. Soc.* **111,** 691 (1984).
18. K. L. Coulson, *Solar and Terrestrial Radiation: Methods and Measurements*, Academic Press, New York, NY (1975).
19. K. N. Liou, *An Introduction to Atmospheric Radiation*, Academic Press, New York, NY (1980).
20. R. A. McClatchey, W. S. Benedict, S. A. Clough, D. E. Burch, R. F. Calfee, K. Fox, L. S. Rothman, and J. S. Garing, AFCRL report AFCRL-TR-73-0096, Air Force Cambridge Research Laboratories, Bedford, MA (1973).
21. L. S. Rothman, R. R. Gamache, A. Goldman, L. R. Brown, R. A. Toth, H. M. Pickett, R. I. Poynter, J.-M. Flaud, C. Camy-Peyret, A. Barbe, N. Husson, C. P. Rinsland, and M. A. H. Smith, *Appl. Opt.* **26,** 4058 (1987).
22. M. D. Chou and A. Arking, *J. Atmos. Sci.* **37,** 855 (1980).
23. M. D. Chou and A. Arking, *J. Atmos. Sci.* **38,** 798 (1981).
24. A. Slingo and H. M. Schrecker, *Q. Jl R. Met. Soc.* **108,** 407 (1982).
25. G. L. Stephens, *Mon. Weath. Rev.* **112,** 826 (1984).
26. G. E. Hunt and I. P. Grant, *J. Atmos. Sci.* **26,** 963 (1969).
27. G. Yamamoto, M. Tanaka, and S. Asano, *JQSRT* **11,** 697 (1971).
28. W. J. Wiscombe and J. W. Evans, *J. Comp. Phys.* **24,** 416 (1977).
29. W. M. Irvine, *Bull. Astr. Insts Neth.* **17,** 266 (1964).
30. S. Bakan and H. Quenzel, *Beitr. Phys. Atmos.* **49,** 272 (1976).
31. S. Bakan, P. Koepke, and H. Quenzel, *Beitr. Phys. Atmos.* **51,** 28 (1978).
32. R. Goody, *Atmospheric Radiation*, Oxford University Press, Oxford (1964).
33. J. P. Blanchet, *Tellus* **37B,** 197 (1985).
34. F. X. Kneizys, E. P. Shettle, W. O. Gallery, J. H. Chetwynd, Jr., L. W. Abreu, J. E. A. Selby, S. A. Clough, and R. W. Fenn, AFGL Report No. AFGL-TR-83-0187, Air Force Geophysics Lab, Hanscom AFB, MA (1983).
35. R. Penndorf, *JOSA* **47,** 176 (1957).
36. M. Nicolet, *Planet. Space Sci.* **33,** 1467 (1984).
37. R. A. McClatchey, R. W. Fenn, J. E. A. Selby, F. E. Volz, and J. S. Garing, AFCRL report AFCRL-72-0497, Air Force Cambridge Research Laboratories, Bedford, MA (1972).
38. M. P. Thekaekara and A. J. Drummond, *Nature Phys. Sci.* **229,** 6 (1971).
39. D. Labs and H. Neckel, *Z. Astrophys.* **69,** 1 (1968).
40. *ICRCCM: Longwave Clear-sky Calculations*, WCP Report No. 93, Geneva (1984).
41. M. D. Chou and L. Peng, *J. Atmos. Sci.* **40,** 2183 (1983).
42. A. Arking and K. Grossman, *J. Atmos. Sci.* **29,** 937 (1972).